Personal Account

THE CHEMICAL RECORD

DOI: 10.1002/tcr.202000090

Graphene Oxide Quantum Dot-Based Functional Nanomaterials for Effective Antimicrobial Applications

Forrest Nichols and Shaowei Chen*[a]

Abstract: Conventional β-lactam antibiotics are resisted by bacteria at an increasing rate, prompting studies into the development of alternate antibiotic agents. In this personal account, we summarize recent progress in the design and engineering of graphene oxide quantum dot-based nanomaterials as potent antimicrobial agents. Specifically, we examine the impacts of chemical reduction on the antimicrobial activity of graphene oxide quantum dots, and enhancement of the bactericidal performance by the formation of nanocomposites with metal oxide nanoparticles, within the context of photodynamic generation of reactive oxygen species. A perspective is also included where the promises and challenges are highlighted in the development of high-performance antimicrobial agents based on graphene derivatives.

Keywords: graphene oxide quantum dot, metal oxide, nanocomposite, photodynamic, antimicrobial

1. Introduction

Antibiotic resistance is becoming increasingly common around the world and threatening the well-being of humanity.[1–4] In particular, β-lactam antibiotics are the most frequently prescribed antibiotic in hospital settings; however, bacteria are able to produce enzymes known as β-lactamases that result in bacterial resistance.[5] Significant research has therefore been dedicated to developing alternate antibiotic agents that can overcome the bacteria's resistance through unique bactericidal pathways. One such alternate route includes the use of graphene-based nanomaterials capable of inhibiting bacterial growth through mechanisms such as physical adsorption and confinement, disruption of cellular processes, and membrane damage through physical and chemical interactions. Furthermore, some forms of functionalized graphene show semiconductor characteristics making these materials light sensitive and capable of photocatalyzing the formation of reactive oxygen species (ROS), such as superoxide (O_2^-), singlet oxygen ($O_2^{\bullet}$), hydroxyl radical ($^{\bullet}OH$), and hydrogen peroxide (H_2O_2),[6–8] that are known to be potent antimicrobial reagents involving various destructive pathways, such as degradation of bacterial DNA and cell wall damage.[9] It is inherently difficult for bacteria to overcome such destructive mechanisms of attack and therefore less likely for the bacteria to gain resististance against ROS-generating nanomaterials.

Graphene derivatives represent a diverse class of carbon functional materials, including an exfoliated version of graphite called graphene, oxidized graphene called graphene oxide (GO), and a partially reduced form of GO called reduced graphene oxide (rGO).[10–17] These materials have been shown to be effective antimicrobial agents on their own, and the antimicrobial activity can be further enhanced when combined with other materials to form a composite, notably with metal nanoparticles, metal oxide nanoparticles, and more recently with atomically dispersed metal atoms.[18] By tailoring the synthesis methods of the graphene-based materials, one can control the size, shape, and degree of oxidation to enhance water solubility, bacterial membrane contact, semiconductor properties, and other important properties for maximal antimicrobial performance.[19,20]

Graphene-based nanomaterials can be prepared through numerous methods, which mostly fall into two categories,

[a] *F. Nichols, Prof. Dr. S. Chen*
Department of Chemistry and Biochemistry
University of California
1156 High Street
Santa Cruz, California 95064, United States
E-mail: shaowei@ucsc.edu

namely, top-down and bottom-up routes, as depicted in Figure 1. In the top-down synthesis of graphene-based nanomaterials, the starting material is usually some form of bulk graphite and then broken down through physical or chemical processes, where exfoliation ultimately results in the production of small graphitic carbon consisting of a varied number of graphene layers. One such top-down method is known as the Hummers' method,[22,23] in which graphite flakes or pitch carbon fiber can be broken down through chemical oxidation using concentrated acids, resulting in the formation of GO. Depending on the degree of oxidation, controlled through reaction temperature, time, and acid concentration, one can obtain GO with sizes varied from several hundred nanometers down to the quantum dot regime of only a few nanometers in diameter.[14,24–27] In the bottom-up route, the starting materials involve a small-molecule carbon source (along with any desired heteroatom dopant materials, such as nitrogen and sulfur), which can be polymerized through various methods involving reduction and condensation reactions. For instance, thermal treatment of citric acid or trisodium citrate at high temperatures in a closed autoclave can be used to produce GO. Under these reaction conditions, citric acid goes through multiple dehydration reactions, resulting in the formation of graphitic carbon nanomaterials with the size regulated by the reaction conditions.[13,17,28,29]

Graphene-based composite materials have shown significant promise for antimicrobial applications. Previous reports include incorporation of graphene derivatives with metals, metal oxides, simple complexes, and other semiconducting photocatalysts.[19,30,31] One of the intriguing aspects of this approach is taking advantage of the semiconductor properties of small graphene derivatives through the creation of semiconductor heterojunctions. For example, we have recently reported on a graphene oxide quantum dot (GOQD)/ZnO composite photocatalyst for bacterial control.[29] The formation of composite materials was shown to improve the dispersibility of ZnO in aqueous media and significantly increase the efficiency of ROS production, likely due to improved contact with the bacterial membrane and enhanced charge separation of the photoexcited electron-hole pairs.

In this personal account, we summarize recent progress in the use of GOQD-based functional nanomaterials for effective antimicrobial applications within the context of photodynamic manipulation. Synthesis of these materials is realized through a top-down or bottom-up approach (Figure 1). The structural characteristics of these materials are unraveled by a range of microscopic and spectroscopic measurements and correlated to the antimicrobial activity towards both Gram-positive and Gram-negative bacteria. Mechanistic insights are obtained by a careful comparison of the bactericidal performance in the dark and under photoirradiation.

2. Graphene Oxide Quantum Dots

Graphene-based materials have been under study for microbial control for more than a decade. In an early study,[32] the antimicrobial properties of graphene and GO were examined

Forrest Nichols received his B.S. degree in Chemistry in 2017 from the University of California, Santa Cruz (UCSC), and continued his studies with Professor Shaowei Chen at UCSC to pursue a Ph.D. degree. His research interests focus on the design, synthesis and engineering of carbon-based nanocomposites for electrocatalysis and antimicrobial applications. Forrest is a first-generation college graduate and aspires to become a professor and promote first-generation student advancement.

Shaowei Chen received his B.S. degree in Chemistry from the University of Science and Technology of China in 1991, and his M.S. and Ph.D. degrees from Cornell University in 1993 and 1996, respectively. Following a postdoctoral appointment at the University of North Carolina at Chapel Hill, he started his independent career in Southern Illinois University in 1998. In 2004, he moved to UCSC. He is currently a professor of chemistry and the faculty director of the UCSC COSMOS program. His research interests are primarily focused on high-performance catalysts for electrochemical energy conversion and storage, impacts of core-ligand interfacial bonding interactions on nanoparticle charge-transfer dynamics, Janus nanoparticles by interfacial engineering, and antimicrobial activity of functional nanocomposites.

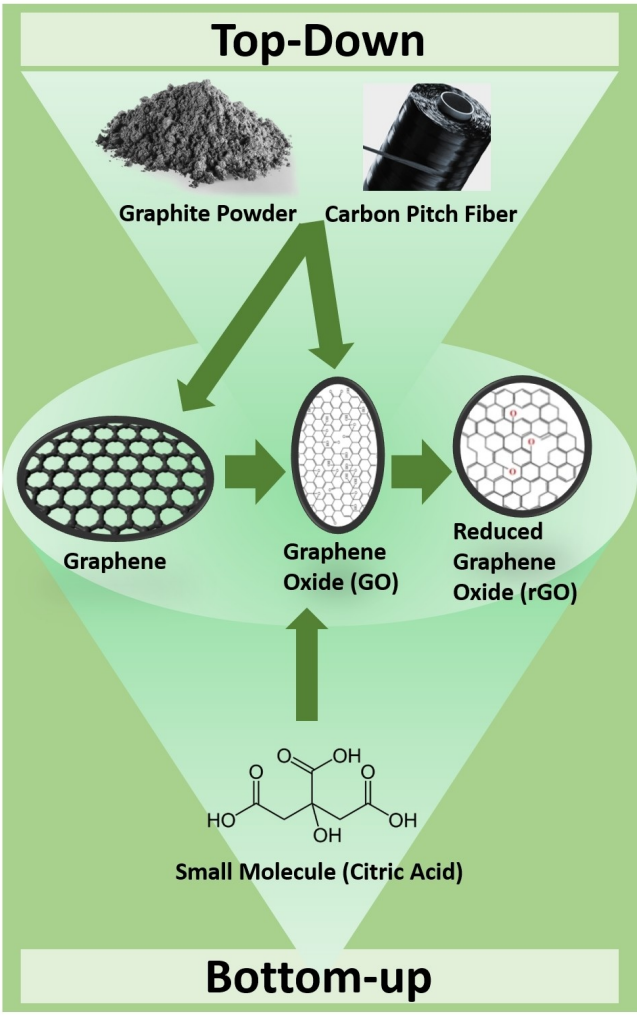

Figure 1. Schematic representation of the preparation of graphene derivatives by the top-down and bottom-up approaches.

and compared toward both Gram-positive and Gram-negative strains of bacteria. Experimentally, GO was synthesized through a (top-down) modified Hummers' method using graphite powders as the starting materials. A graphene nanowall array was then grown onto a stainless-steel substrate by electrophoretic deposition. It was observed that membrane damage caused by the sharp edges of the GO nanosheets was the primary mechanism of bacterial control. This explanation was supported by the resistance of *Escherichia coli* (*E. coli*), a Gram-negative bacterial strain with a developed outer membrane, as compared to the Gram-positive strain of *Staphylococcus aureus* (*S. aureus*), which lacks the protective outer membrane.

This proposed mechanism was further built upon through the study of the antimicrobial activity of graphite, graphite oxide, GO, and rGO.[33] The interactions of these carbon materials with *E. coli* cells were investigated by scanning electron microscopic (SEM) studies and the material's ability to oxidize glutathione was quantitatively assessed – note that glutathione is a common redox mediator in bacterial cells. The conclusions from the previous report[32] were validated, as SEM images clearly showed cell membrane damage caused by the sharp edges of the GO nanosheets.

Oxidative stress also plays an important role, as GO can induce substantial glutathione oxidation, in comparison to other graphene derivatives, and glutathione deficiencies have been known to impact cell growth, due to unregulated potassium channels and sensitivity to methylglyoxal, a toxic byproduct of bacteria metabolism.[34] Notably, results from earlier studies have shown that a decreasing lateral size of GO prepared through a modified Hummers' method resulted in an increase of the antibacterial activity,[35,36] as evidenced in a range of characterizations based on fluorescence microscopy, glutathione oxidation, and cell viability assays, where smaller GO was found to exhibit more oxidative stress toward *E. coli.* Results from these studies further solidify the importance of oxidative stress in the bactericidal action of graphene-based nanomaterials.

Such oxidative stress most likely arises from the rich oxygenated functional moieties on the GO surface, which can be readily manipulated by chemical reduction. In a recent study,[27] ultrasmall GO nanosheets, also known as GOQD,[24,25,37–39] were prepared by a modified Hummers' method using pitch carbon fibers as the starting materials, and the antimicrobial activity was examined and compared before and after chemical reduction by $NaBH_4$. Figure 2a depicts a representative transmission electron microscopic (TEM) image of the as-produced GOQD, which exhibited a diameter of 10 to 20 nm and clear lattice fringes, with an interplanar spacing of 0.263 nm that is consistent with that of the graphene (002) lattice. Topographic study based on atomic force microscopy (AFM) shows good dispersion of the GOQD without apparent agglomeration, most likely due to the abundant oxygenated moieties on the GOQD surface that rendered the GOQDs dispersible in water, and from the line scan, the height of the GOQDs was found to range from 0.5 to 2 nm, corresponding to 1 to 4 graphene layers. The morphology of the reduced form (rGOQD) was largely unchanged.[27]

Yet the optical and photoluminescence characteristics varied rather markedly after $NaBH_4$ reduction. From the UV-vis absorption spectra in Figure 2b, one can see that GOQD exhibited a major absorption peak at 230 nm, and three broad shoulders at 290, 360, and 460 nm (marked by asterisks) on an exponential decay profile. Note that the 230 nm peak is generally ascribed to the $\pi \rightarrow \pi^*$ transitions of sp^2 carbon, and the 460 nm one to the $n \rightarrow \pi^*$ transitions of C=O moieties.[40–42] After $NaBH_4$ reduction, the 230 nm peak red-

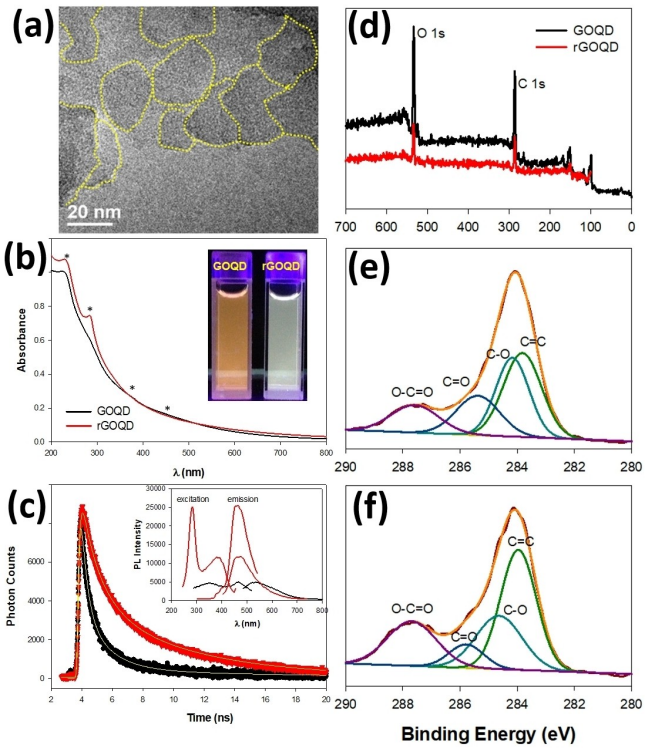

Figure 2. (a) TEM image of GOQD. Scale bar 20 nm. (b) UV-vis absorption spectra of GOQD (black) and rGOQD (red) in water. Inset shows the photographs of the two solutions under photoirradiation at 365 nm. (c) TRPL emission spectra for GOQD (black) and rGOQD (red) at the excitation of 400 nm. Yellow lines are the exponential decay fits. Inset shows the corresponding SSPL emission spectra. (d) XPS survey spectra of GOQD (black) and rGOQD (red). High resolution XPS spectra of the carbon 1 s electrons for (e) GOQD and (f) rGOQD. Reproduced with permission from ref. 27, copyright 2020, the authors.

shifted and the 460 nm one disappeared, suggesting enlarged sp^2 carbon domains in rGOQD, most likely due to effective removal of oxygenated species. In fact, based on the Tauc plots derived from the UV-vis absorption profiles, the optical band gap can be found to decrease somewhat from 3.50 eV for GOQD to 3.15 eV for rGOQD. Consistent results were obtained in ^{1}H NMR measurements where signals of aromatic protons were found to intensify with rGOQD, as compared to that of GOQD.[27]

The photoluminescence properties varied accordingly, as manifested in the photographs of the sample solutions under 365 nm photoirradiation, yellow-green for GOQD and blue-green for rGOQD (Figure 2b inset). In steady-state photoluminescence (SSPL) measurements (Figure 2c inset), GOQDs exhibited two excitation peaks (λ_{ex}) centered at 350 and 465 nm, very close to the absorption peak positions observed in UV-vis measurements (Figure 2b), and a corresponding emission peak (λ_{em}) at 535 nm. However, upon $NaBH_4$ chemical reduction, the excitation peak at 465 nm vanished, a new excitation peak appeared at 280 nm, and the emission band blue-shifted to 460 nm, with the normalized emission intensity more than doubled. Consistent behaviors were observed in time-resolved photoluminescence (TRPL) measurements (Figure 2c), where the emission lifetime of the rGOQD was estimated to be 1.73 ns, somewhat longer than that for GOQDs (1.05 ns), in good accord with the removal of structural defects (trap states) upon $NaBH_4$ reduction.[27]

Such a structural evolution is indeed confirmed by X-ray photoelectron spectroscopy (XPS) measurements. From the survey spectra in Figure 2d, one can see that both the GOQD and rGOQD samples exhibited two main peaks at 284 eV for C 1s and 530 eV for O 1s electrons, and based on the integrated peak areas, the oxygen content of rGOQD diminished by more than 10%, as compared to that of GOQD, suggesting effective removal of oxygen species by $NaBH_4$ reduction. Deconvolution of the high-resolution C 1s spectra for GOQD (Figure 2e) and rGOQD (Figure 2f) further reveals the difference in oxygen functional groups within the carbon framework. Whereas four components can be resolved in both samples at 282.8, 284.2, 285.4, and 287.6 eV, corresponding to C=C, C–O, C=O, and O–C=O, respectively, the contents of the oxygenated species decrease rather markedly, carbonyl species from 19.2% in GOQD to 8.3% in rGOQD, and C–O from 29.7% to 25.1%, and concurrently the fraction of sp^2 carbon increases from 36.2 for GOQD % to 44.1% for rGOQD.

The clear difference in the contents of oxygen functional groups between GOQD and rGOQD provided an excellent platform to examine what roles these oxygen moieties play in microbial inactivation. To quantify the antimicrobial properties of these materials a photodynamic experiment involving plate streaking was implemented. A typical procedure for this type of experiment is as follows: briefly, the material of interest is dissolved in a desired solvent, typically water or phosphate buffered saline (PBS), into which an amount of cultured bacteria is added and shaken to form a homogeneous solution. Use of a buffer solution is particularly critical when the material of interest has the ability to significantly alter the experimental pH conditions, as seen previously when GO containing acidic impurities was used.[43] The resulting solution is then irradiated at the desired photon energy for a specific time interval. At each timepoint a small aliquot is taken from the solution, serially diluted, and streaked onto an agar plate. The plates are then incubated typically at 37 °C for 16–24 h, depending on the microbe under study. The incubated plate is then taken, and individual colonies are counted and compared. Control plates are typically made to efficiently compare difference in colony formation. For example, the bar chart in Figure 3a demonstrates a clear difference in photoinactivation between GOQD and rGOQD, as compared to a control group using water alone.

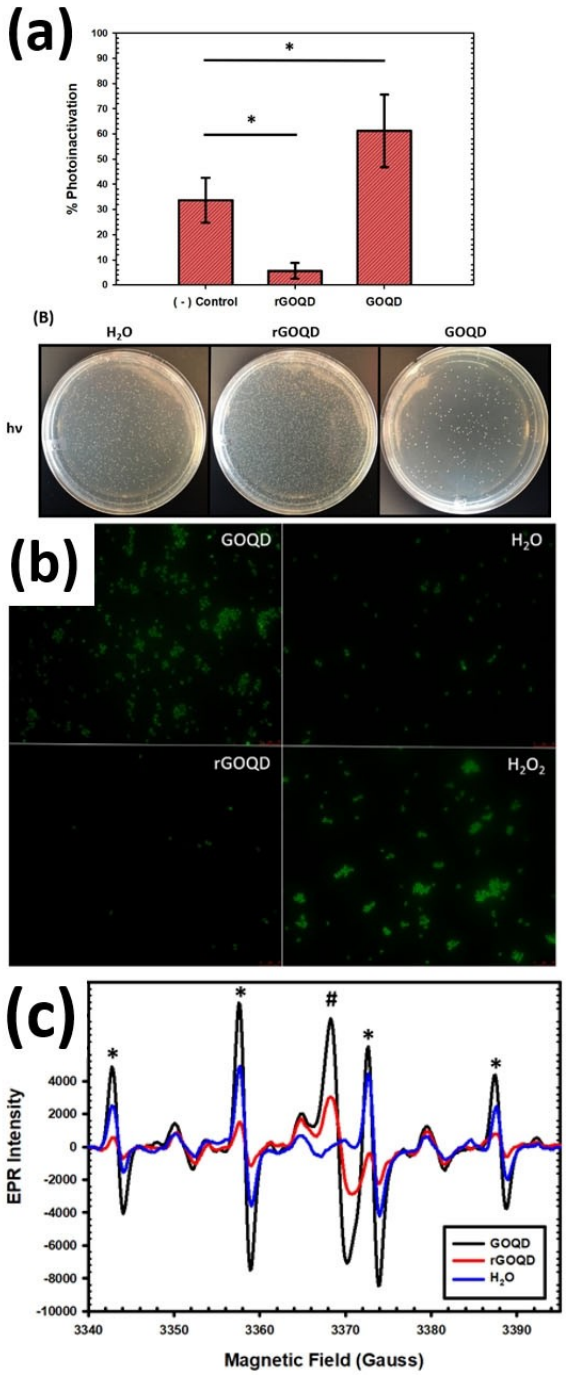

Figure 3. (a) Results of photodynamic experiments depicting the photoinactivation (%) of *S. epidermitis* by GOQD and rGOQD. (b) Fluorescence microscopy images of CellROX green-stained *S. epidermitis* bacterial cells in the presence of GOQD (top-left panel), rGOQD (bottom-left panel), H_2O (as a negative control, top-right panel), and H_2O_2 (as a positive control, bottom-right panel). (c) EPR spectra of GOQD (black), rGOQD (red), and blank water (blue) under photoirradiation (400 nm) for 1 min in the presence of DMPO. Reproduced with permission from ref. 27, copyright 2020, the authors.

The photodynamic experiment described above is useful to quantify antibacterial properties as a function of photoirradiation. Experimentally, each sample was exposed to light irradiation (400 nm) for 3 min and changes in cell viability were measured through colony counts. From the top panel of Figure 3a, one can see a ca. 60% loss of cell viability with *Staphylococcus epidermitis* (*S. epidermitis*) in the presence of GOQD upon photoirradiation, in comparison to ca. 35% in the control, while 95% of the bacterial cells survive with rGOQD. Such a difference of the cell viability can also be readily visualized in the corresponding photographs of bacterial colonies in the bottom panel. It is likely that the rGOQD possesses surface functional groups with antioxidant nature resulting in improved cell viability under 400 nm light irradiation. The source of this antioxidant behavior is likely due to the increased sp^2 carbons in rGOQD, which can undergo hydroxyl addition in the presence of radical species.

Fluorescence microscopy studies, in conjunction with electron paramagnetic resonance (EPR) spectroscopy, indeed provide an adequate foundation to understand the mechanisms for ROS formation upon light irradiation. Figure 3b depicts fluorescence micrographs of CellROX green-stained *S. epidermitis* bacterial cells in the presence of GOQD (top-left panel), rGOQD (bottom-left panel), a hydrogen peroxide positive control (bottom-right panel), and water alone as a negative control (top-right panel). CellROX green is a dye molecule that binds to nucleic acids with a primary binding to DNA after oxidation. Upon oxidation and dye accumulation within the cell, CellROX green emissions can be observed at 525 nm with an excitation wavelength of 470 nm. The resulting fluorescence intensity can be normalized and compared between samples to quantify the degree of ROS production where an increased fluorescence intensity is correlated to an increased amount of ROS produced. From Figure 3b, one can see a 2-fold increase in CellROX green intensity for GOQD, as compared to that for rGOQD — the former is actually comparable to that with H_2O_2 whereas the latter is similar to that of H_2O. Such a clear increase in ROS production by GOQD can be correlated to the rich oxygenated species, as evidenced in XPS measurements (Figure 2d-f).

Consistent results were obtained in EPR measurements.[44] The studies described herein utilize a spin-trapping method where 5,5-dimethyl-1-pyrroline N-oxide (DMPO) is oxidized at the nitrone functional group by free radicals to form a radical adduct with a half-life ($\tau_{1/2}$) on the order of several minutes. This allows for reliable detection of free radicals formed by the photocatalyst of interest. Figure 3c depicts such spin-trapping assays in which DMPO reacts with radicals formed by GOQD and rGOQD upon photoirradiation for 1 min, along with a control group containing water alone. The EPR spectra show a peak (marked by #) at 3369 G for GOQD and rGOQD, as compared to the water control, and

the scaling factor (g) was estimated to be 2.0034 ± 0.0005 for GOQD and rGOQD, which lies between the literature values of 2.0023 for carbon-centered radicals and 2.004 for oxygen-centered radicals.[45,46] From Figure 3c, one can see that GOQD is producing significantly more of these radicals than rGOQD with a peak height nearly double that of rGOQD. This can be ascribed to chemical reduction of GOQD to rGOQD that removes the oxygenated moieties necessary for such radical formation. Furthermore, formation of a quartet (depicted by asterisks) is seen with an intensity ratio of 1:2:2:1 and hyperfine couplings of $a_N = a_H = 14.9$ G, characteristic of hydroxyl radical adducts to DMPO. From the peak intensity of these quartets, one can see a 7-fold increase for GOQD, as compared to that of rGOQD, further confirming that radical formation was hindered after $NaBH_4$ reduction, likely due to the removal of oxygen moieties necessary for radical formation from the GOQD surface.

These results suggest that the antimicrobial activity of graphene derivatives may arise from multiple contributions. In addition to physical damage of the cell membranes, graphene-based nanomaterials can effectively inhibit bacterial cell growth by ROS production, which is closely related to the oxygen functional moieties. Further enhancement of the bactericidal performance can be achieved by the formation of nanocomposites with select metal oxide nanoparticles, as detailed below.

3. Graphene Oxide Quantum Dots/Metal Oxide Nanocomposites

Incorporation of graphene-based materials with metal or metal oxide nanostructures to produce nanocomposites has been rather extensively studied toward efficient antimicrobial activity.[16] The key to a successful composite material largely relies on (i) a sufficient contact between the graphene-based material and metal (oxide) nanostructures and (ii) biocompatibility of the latter. Silver has been a common metal of choice. For instance, silver nanoparticles have been deposited on rGO and the resulting Ag/rGO nanocomposite was found to display improved antibacterial activity, as compared to silver alone; and the activity is even comparable to that of ampicillin, a penicillin group β-lactam antibiotic.[47] Efficient control of the growth of Gram-positive and Gram-negative bacterial strains has also been observed with Ag/GO nanocomposites.[48]

For metal oxide/graphene nanocomposites, the antimicrobial performance can be further enhanced by taking advantage of the photochemical activity of the semiconducting metal oxides. This is because upon photoirradiation of a semiconductor with photons of an appropriate energy, electrons may be excited from the valence band to the conduction band, and the ensuing separation of the photogenerated electron-hole pairs can be exploited for a range of reduction/oxidation reactions, in particular, ROS production for antimicrobial applications.[49–51] In addition, the incorporation of graphene derivatives helps improve the dispersibility, charge transfer, and other aspects pertinent to ROS production.[16] Zinc oxide (ZnO) is a commonly used photocatalyst with a direct bulk band gap of 3.3 eV at room temperature.[52] Beyond its unique band structure, ZnO is highly desirable for antimicrobial applications due to its low cost, high stability, and biocompatibility.[53] For example, ZnO nanoparticles have been deposited on rGO for water disinfection via the ROS mediated pathway.[54] Experimentally, two samples were prepared, one with ZnO nanoparticles in the range of 20 nm to 100 nm and the other from 50 nm to 500 nm. Through photodegradation of methylene blue and photoreduction of Cr (VI) to Cr(III), it was clear that a reduced ZnO nanoparticle size resulted in an improved photocatalytic performance, which was ascribed to improved ZnO/rGO interfacial contact and thus enhanced photodegradation efficiency.

As previously mentioned, use of GO over rGO may substantially improve the material's ability to form ROS under photoirradiation. To this end, we have recently constructed ZnO/GOQD nanocomposites utilizing a bottom-up procedure, where GOQDs were thermally derived from citric acid followed by the deposition of ZnO nanoparticles.[17] The ZnO nanoparticles, with the particle size ranging from 5 to 12 nm in diameter and an average diameter of $8.37 \text{ nm} \pm 2.72$ nm (markedly smaller than those in the literature[54]), were successfully deposited onto the as-prepared GOQD surface. Figure 4a depicts the UV-vis absorption and photoluminescence emission spectra of the ZnO/GOQD nanocomposite, ZnO nanoparticles, and GOQDs alone.[17] One can see that despite similar UV-vis absorption profiles, the photoluminescence emission intensity varied markedly among the samples. Specifically, significant quenching can be observed with the ZnO/GOQD composite, as compared to the as-prepared GOQD alone. This suggests a reduced recombination of photogenerated electron-hole pairs upon ZnO deposition, likely due to charge transfer occurring from the GOQD to the ZnO at the ZnO/GOQD interface.

Indeed, the ZnO/GOQD composite possessed markedly enhanced ROS production. EPR measurements in Figure 4b show a typical quartet (marked by asterisks) that is indicative of the formation of hydroxyl radicals, as well as three doublets with hyperfine splitting of $a_H = 15.6$ G and $a_N = 22.9$ G, corresponding to $H^{\bullet}$ formation likely produced by ZnO photoreduction of water. These EPR results help explain the significantly improved antibacterial properties of ZnO/GOQD shown in Figure 4d, which depicts results from a photodynamic assay of the colony forming units (CFU) under UV light irradiation. The ZnO/GOQD composite (yellow diamonds) displays complete bacterial inactivation after a photo-

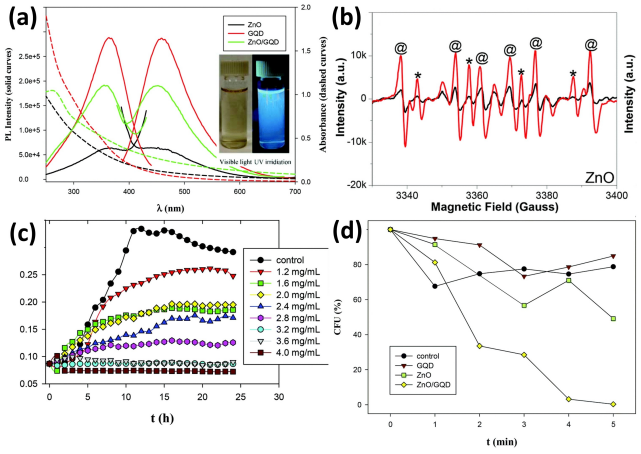

Figure 4. (a) UV-vis (dashed curves) and SSPL (solid curves) spectra of ZnO (black), GOQD (red), and ZnO/GOQD composite (green). Inset depicts the color of the ZnO/GOQD solution under UV (365 nm) and visible light photoirradiation. (b) EPR spectra of water control (black) and ZnO/GOQD nanocomposite (red) under photoirradiation (365 nm) for 1 min. (c) Bacterial growth at varying concentrations of the ZnO/GOQD composite from 0 mg/mL (black) to 4.0 mg/mL (red square) performed in the dark for 24 h. Measurements are taken from light absorption at 600 nm for each timepoint. (d) Results from photodynamic experiments plotting colony forming units (CFU) versus irradiation time (min). Reproduced with permission from ref. 17, copyright 2018, the Royal Society of Chemistry.

irradiation period of only 5 min. This is a significant improvement from the control sample containing only *E. coli* and water (black circles), GOQD (red triangles), and ZnO (green squares). This clearly demonstrates the improved antibacterial properties of the composite made by the GOQD and ZnO. Note that the activity is also markedly better than those observed with similar composites but consisting of larger ZnO nanoparticles,[54] likely due to the combined contributions of enhanced dispersion and interfacial charge transfer. In contrast, microbial growth in the dark requires significantly more material to sufficiently stop bacterial growth (Figure 4c), suggesting photocatalyzed production of $OH^{\bullet}$ as the primary mechanism responsible for the antibacterial properties of the ZnO/GOQD composite.

It has long been argued that sufficient contact with the bacterial membrane is critical for efficient antibacterial performance.[19,55,56] Indeed, the importance of membrane contact with GO basal planes has been highlighted.[57] For example, bacterial membrane contact was enhanced with a ZnO/GO composite, leading to improved bactericidal activity, as compared to ZnO particles alone.[58] It was hypothesized that GO incorporation facilitated the dispersion of ZnO nanoparticles, slowed the dissolution of ZnO, and enabled intimate contact with *E. coli* cell membranes. This was evidenced by SEM imaging and solubilization measurements in which the prepared nanocomposites were dispersed in culture media for 24 h with periodic quantification of released Zn. This highlights the importance of nanocomposite dispersibility and bacterial membrane contact in the bactericidal efficiency.

One route toward increased dispersion, and hence improved antibacterial activity, involves the incorporation of hydrophilic polymers into the antimicrobial agents. In an early study,[59] GO was synthesized from graphite powders through a modified Hummers' method, and functionalized with a guanidine polymer (GP) by mixing GO, polyethylene glycol (PEG), and GP at elevated temperatures. The resulting GO-PEG-GP nanocomposite displayed structural characteristics similar to those of GO, as evidenced in FTIR, SEM, TGA (thermogravimetric analysis), and XRD (X-ray diffraction) measurements, but with significantly improved water dispersibility even after prolonged periods of time. The antimicrobial activity towards *E. coli* and *S. aureus* bacteria was then evaluated by counting the CFUs after an incubation period. It was found that after 60 min the GO-PEG-GP composite led to complete bacterial inactivation for both the Gram-positive and Gram-negative strains, resulting from improved GO dispersion and microbe contact. In another study,[60] Cu_2O/rGO nanocomposites were prepared in the presence of PEG, which exhibited enhanced dispersibility and stability in water and facilitated ROS production, leading to excellent antibacterial activity towrds *E. coli* and *S. aureus*, in comparison to Cu_2O nanoparticles alone.

Bridging previous reports on nanoparticle dispersion and an understanding of bacteria surface charge, we demonstrated that the bacteria surface charge can indeed be exploited for further improvement of membrane contact and bacterial inactivation.[29] Experimentally, cationic polyethylenimine (PEI) was used as the capping polymer to further functionalize the ZnO/GOQD nanocomposites,[17] as schematically depicted in Figure 5a. The obtained ZnO/GOQD-PEI composite exhibited a positively charged surface, which was anticipated to possess electrostatic attraction toward the negatively charged surface of Gram-negative *E. coli* membranes. This was indeed evidenced in ζ-potential measurements (Figure 5b). One can see that incorporation of PEI shifted the ζ-potential from −40.4 mV for ZnO/GOQD to +16.67 mV for the ZnO/GOQD-PEI composite, and the ZnO/GOQD-PEI composites displayed significantly improved dispersibility for up to 48 h, as compared to ZnO/GOQD alone. This can be ascribed to increased hydrophilicity with the PEI coating.

Similarity in morphology and atomic composition was further evidenced in XRD measurements, where both samples displayed closely similar patterns attributed to hexagonal wurtzite ZnO (JCPDS No. 36-1451) with six signature peaks occurring at $2\theta = 31.77°$, 34.42°, 36.25°, 47.54°, 56.60°, and 62.86°. Furthermore, PEI incorporation improved the nanocomposite's ability to form ROS as manifested in EPR

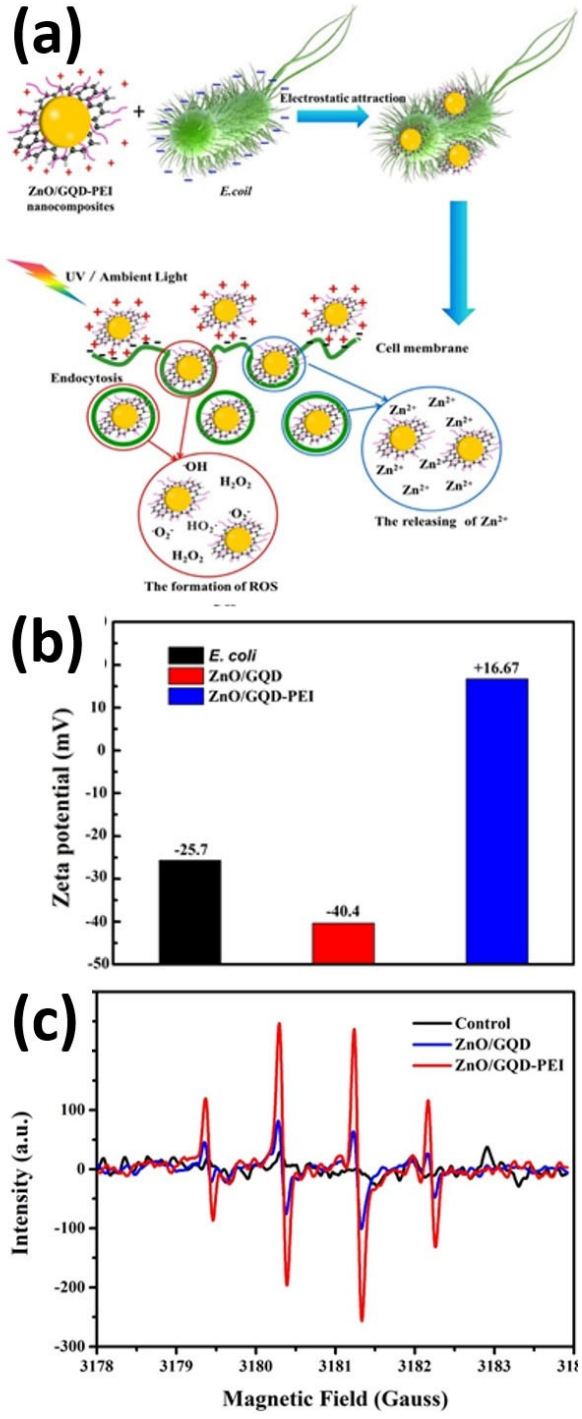

Figure 5. (a) Schematic representation of ZnO/GOQD-PEI antibacterial mechanism. (b) ζ-potentials of *E. coli* (black), ZnO/GOQD (red), and ZnO/GOQD-PEI (blue). (c) EPR spectra of ZnO/GOQD (blue), ZnO/GOQD-PEI (red), and water alone with the addition of DMPO after light irradiation for 1 min. Reproduced with permission from re. 29, copyright 2019, the American Chemical Society.

measurements. Figure 5c depicts the EPR data, again, utilizing DMPO as the spin trapping agent. One can see the formation of a quartet with the peak intensity ratio of 1:2:2:1 in the range of 3179 to 3183 G for both ZnO/GOQD and ZnO/GOQD-PEI samples, as compared to the control group containing water and DMPO alone. This is the clear signature of hydroxyl radical formation upon light irradiation. Further comparing the quartet peak intensity between both samples, a 3-fold increase in ROS generation can be observed for ZnO/GOQD-PEI, as compared to ZnO/GOQD.

The antibacterial activity of the two samples was then carried out in both dark and light conditions. Figure 6 depicts the growth of *E. coli* cells in the dark in the presence of (a) ZnO/GOQD and (b) ZnO/GOQD-PEI. From these spectra, a minimum inhibitory concentration (MIC) can be estimated for each sample, 4.0 mg/mL for ZnO/GOQD, and 2.7 mg/mL for ZnO/GOQD-PEI. This suggests an improved antibacterial control with the incorporation of PEI, possibly due to the increased dispersion of particles as evidenced above. Next, the antibacterial activity under photoirradiation was characterized, with results presented in Figure 6c. Based on the results from the dark conditions, the nanocomposite concentration was set at 2.0 mg/mL for all photodynamic experiments, below the MIC found for both samples. From Figure 6c, both ZnO/GOQD and ZnO/GOQD-PEI can be observed to exhibit apparent bactericidal activity, as compared to the control, and most notably, the performance was markedly enhanced with ZnO/GOQD-PEI, as compared to ZnO/GOQD. In fact, complete bacterial inactivation was achieved at an irradiation time of 5 min for ZnO/GOQD-PEI. The improved antibacterial activity under UV irradiation can be attributed to the electrostatically enhanced contact between the nanocomposite and bacterial cells which led to improved bacterial decomposition by Zn^{2+} dissolution and ROS degradation.

4. Summaries and Perspectives

The antimicrobial activity of graphene derivatives can arise from multiple mechanisms of actions, such as membrane damage by the sharp edges of the graphene nanosheets, nutrient deprivation of bacterial cells due to graphene encapsulation, as well as ROS production facilitated by the rich oxygen moieties within the graphene framework. Thus, one can envision that chemical reduction/oxidation can be exploited as a facile strategy to manipulate the surface functional groups and hence the bactericidal performance. Further enhancement of the antimicrobial activity can be achieved by the formation of nanocomposites with select metal oxide nanoparticles by taking advantage of the unique photocatalytic activity. Notably, incorporation of graphene deriva-

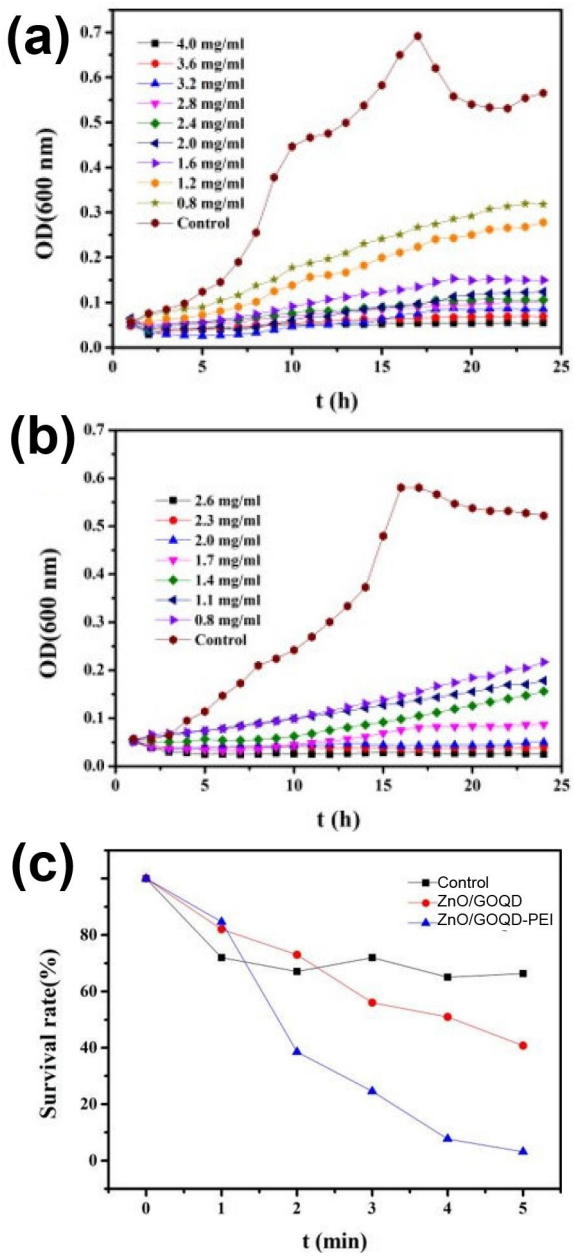

Figure 6. *E. coli* growth assays performed in the dark with (a) ZnO/GOQD and (b) ZnO/GOQD-PEI over a 24 h period at varying nanocomposite concentrations ranging from 0.8–4.0 mg/mL. (c) Photodynamic experiments performed under UV irradiation with ZnO/GOQD (red circles) and ZnO/GOQD-PEI (blue triangles) over a 5 min period, in comparison to the control (black squares). Reproduced with permission from ref. 29, copyright 2019, the American Chemical Society.

tives to the composite system not only helps improve the dispersibility and stability of the nanocomposite in water, but also facilitates ROS generation through interfacial charge transfer. Additionally, the composite's surface charge can be exploited to increase electrostatic attraction between the nanocomposite and bacterial membrane resulting in improved interfacial contact and delivery of photocatalyzed ROS.

Despite substantial progress in recent research, several challenges remain. First, it remains challenging, and yet particularly important, to precisely control the GOQD size, surface morphologies, and oxygen functionalization, which has been known to affect ROS production and oxidative stress. To this end, new synthetic chemistry needs to be developed for the ready control of the GOQD dimensions and structures, as well as the specific oxygenated functional moieties. Second, there are many factors that can contribute to the overall antimicrobial activity of these materials. To parse the contributions from each of these factors and develop a holistic interpretation of the antibacterial mechanism of the material, analysis in real time (in vivo) will be needed to deconvolute the antimicrobial activity occurring on different time scales. For example, ROS related bacterial death occurs at a much shorter time scale (typically within min), as compared to bacterial growth dynamics that occur throughout several hours. Finally, a multidisciplinary approach must be taken to unravel the biological origin of bacterial cell death. There are numerous biological assays that have the potential to significantly improve our understanding of the bacteria-graphene interactions and the impacts on important biochemical processes within the bacterial cell. For example, metabolite screening may be used to quantify changes in microbial metabolism in the presence of ROS generating materials, which has the potential to provide substantial insights into the mechanism of action for graphene-based materials as well as many other prospective antimicrobial nanomaterials.[61,62] Research along these lines is ongoing.

Acknowledgements

The authors thank Mr. P. S. Li for the assistance of the artistic design of the graphic abstract. This work was supported by the US National Science Foundation (CBET-1848841).

References

[1] K. Y. Zheng, M. I. Setyawati, D. T. Leong, J. P. Xie, *Coord. Chem. Rev.* **2018**, *357*, 1–17.
[2] L. J. V. Piddock, *Lancet Infect. Dis.* **2012**, *12*, 249–253.
[3] E. Y. Klein, T. P. Van Boeckel, E. M. Martinez, S. Pant, S. Gandra, S. A. Levin, H. Goossens, R. Laxminarayan, *Proc. Natl. Acad. Sci. USA* **2018**, *115*, E3463-E3470.
[4] S. R. Partridge, S. M. Kwong, N. Firth, S. O. Jensen, *Clin. Microbiol. Rev.* **2018**, *31*, e00088–17.
[5] K. Bush, P. A. Bradford, *Nat. Rev. Microbiol.* **2019**, *17*, 295–306.

[6] R. Kumar, A. Umar, G. Kumar, H. S. Nalwa, *Ceram. Int.* **2017**, *43*, 3940–3961.
[7] K. Z. Qi, B. Cheng, J. G. Yu, W. K. Ho, *J. Alloys Compd.* **2017**, *727*, 792–820.
[8] Y. Nosaka, A. Y. Nosaka, *Chem. Rev.* **2017**, *117*, 11302–11336.
[9] D. J. Dwyer, M. A. Kohanski, J. J. Collins, *Curr. Opin. Microbiol.* **2009**, *12*, 482–489.
[10] T. He, Y. Peng, Q. Li, J. E. Lu, Q. Liu, R. Mercado, Y. Chen, F. Nichols, Y. Zhang, S. Chen, *ACS Appl. Mater. Interfaces* **2019**, *11*, 46912–46919.
[11] W. Yang, G. Chata, Y. Zhang, Y. Peng, J. E. Lu, N. Wang, R. Mercado, J. Li, S. Chen, *Nano Energy* **2019**, *57*, 811–819.
[12] N. Wang, L. Li, N. Zhou, S. Chen, *Phys. Status Solidi B* **2018**, *255*, 1700535.
[13] L. Chen, Y. Peng, J.-E. Lu, N. Wang, P. Hu, B. Lu, S. Chen, *Int. J. Hydrogen Energy* **2017**, *42*, 29192–29200.
[14] C. P. Deming, R. Mercado, J. E. Lu, V. Gadiraju, M. Khan, S. Chen, *ACS Sustain. Chem. Eng.* **2016**, *4*, 6580–6589.
[15] B. Lu, L. Guo, F. Wu, Y. Peng, J. E. Lu, T. J. Smart, N. Wang, Y. Z. Finfrock, D. Morris, P. Zhang, N. Li, P. Gao, Y. Ping, S. Chen, *Nat. Commun.* **2019**, *10*, 631.
[16] M. D. Rojas-Andrade, G. Chata, D. Rouholiman, J. Liu, C. Saltikov, S. Chen, *Nanoscale* **2017**, *9*, 994–1006.
[17] J. Liu, M. D. Rojas-Andrade, G. Chata, Y. Peng, G. Roseman, J.-E. Lu, G. L. Millhauser, C. Saltikov, S. Chen, *Nanoscale* **2018**, *10*, 158–166.
[18] S. Szunerits, R. Boukherroub, *J. Mater. Chem. B* **2016**, *4*, 6892–6912.
[19] H. W. Ji, H. J. Sun, X. G. Qu, *Adv. Drug Delivery Rev.* **2016**, *105*, 176–189.
[20] P. L. Zuo, X. H. Lu, Z. G. Sun, Y. H. Guo, H. He, *Microchim. Acta* **2016**, *183*, 519–542.
[21] S. Priyadarsini, S. Mohanty, S. Mukherjee, S. Basu, M. Mishra, *J. Nanostruct. Chem.* **2018**, *8*, 123–137.
[22] W. S. Hummers, R. E. Offeman, *J. Am. Chem. Soc.* **1958**, *80*, 1339–1339.
[23] P. Rajapaksha, S. Cheeseman, S. Hombsch, B. J. Murdoch, S. Gangadoo, E. W. Blanch, Y. Truong, D. Cozzolino, C. F. McConville, R. J. Crawford, V. K. Truong, A. Elbourne, J. Chapman, *ACS Appl. Bio Mater.* **2019**, *2*, 5687–5696.
[24] X. Fan, B. D. Phebus, L. Li, S. Chen, *Sci. Adv. Mater.* **2015**, *7*, 1990–2010.
[25] C. P. Deming, R. Mercado, V. Gadiraju, S. W. Sweeney, M. Khan, S. Chen, *ACS Sustain. Chem. Eng.* **2015**, *3*, 3315–3323.
[26] K. Liu, Y. Song, S. Chen, *Int. J. Hydrogen Energy* **2016**, *41*, 1559–1567.
[27] M. D. Rojas-Andrade, T. A. Nguyen, W. P. Mistler, J. Armas, J. E. Lu, G. Roseman, W. R. Hollingsworth, F. Nichols, G. Millhauser, A. L. Ayzner, C. Saltikov, S. Chen, *Nanoscale Adv.* **2020**, 2, 1074–1083.
[28] L. Chen, P. Hu, C. P. Deming, N. Wang, J. E. Lu, S. Chen, *J. Phys. Chem. C* **2016**, *120*, 13303–13309.
[29] J. Liu, J. Shao, Y. Wang, J. Li, H. Liu, A. Wang, A. Hui, S. Chen, *ACS Sustain. Chem. Eng.* **2019**, *7*, 16264–16273.
[30] F. Perreault, A. F. de Faria, M. Elimelech, *Chem. Soc. Rev.* **2015**, *44*, 5861–5896.
[31] A. B. Seabra, A. J. Paula, R. de Lima, O. L. Alves, N. Duran, *Chem. Res. Toxicol.* **2014**, *27*, 159–168.
[32] O. Akhavan, E. Ghaderi, *ACS Nano* **2010**, *4*, 5731–5736.
[33] S. B. Liu, T. H. Zeng, M. Hofmann, E. Burcombe, J. Wei, R. R. Jiang, J. Kong, Y. Chen, *ACS Nano* **2011**, *5*, 6971–6980.
[34] L. Masip, K. Veeravalli, G. Georgiou, *Antioxid. Redox Signal.* **2006**, *8*, 753–762.
[35] S. Liu, M. Hu, T. H. Zeng, R. Wu, R. Jiang, J. Wei, L. Wang, J. Kong, Y. Chen, *Langmuir* **2012**, *28*, 12364–12372.
[36] F. Perreault, A. F. de Faria, S. Nejati, M. Elimelech, *ACS Nano* **2015**, *9*, 7226–7236.
[37] G. He, Y. Song, K. Liu, A. Walter, S. Chen, S. Chen, *ACS Catal.* **2013**, *3*, 831–838.
[38] Y. Song, S. Chen, *ACS Appl. Mater. Interfaces* **2014**, *6*, 14050–14060.
[39] W. B. Hu, C. Peng, W. J. Luo, M. Lv, X. M. Li, D. Li, Q. Huang, C. H. Fan, *ACS Nano* **2010**, *4*, 4317–4323.
[40] K. P. Loh, Q. Bao, G. Eda, M. Chhowalla, *Nat. Chem.* **2010**, *2*, 1015.
[41] G. Eda, Y. Y. Lin, C. Mattevi, H. Yamaguchi, H. A. Chen, I. S. Chen, C. W. Chen, M. Chhowalla, *Adv. Mater.* **2010**, *22*, 505–509.
[42] J. Shang, L. Ma, J. Li, W. Ai, T. Yu, G. G. Gurzadyan, *Sci. Rep.* **2012**, *2*, 792.
[43] I. Barbolina, C. Woods, N. Lozano, K. Kostarelos, K. Novoselov, I. Roberts, *2D Mater.* **2016**, *3*, 025025.
[44] S. Suzen, H. Gurer-Orhan, L. Saso, *Molecules* **2017**, *22*, 181.
[45] U. Green, Y. Shenberger, Z. Aizenshtat, H. Cohen, S. Ruthstein, *JOVE-J. Vis. Exp.* **2014**, e51548.
[46] F. Tampieri, S. Silvestrini, R. Riccò, M. Maggini, A. Barbon, *J. Mater. Chem. C* **2014**, *2*, 8105–8112.
[47] W.-P. Xu, L.-C. Zhang, J.-P. Li, Y. Lu, H.-H. Li, Y.-N. Ma, W.-D. Wang, S.-H. Yu, *J. Mater. Chem.* **2011**, *21*, 4593–4597.
[48] J. Tang, Q. Chen, L. Xu, S. Zhang, L. Feng, L. Cheng, H. Xu, Z. Liu, R. Peng, *ACS Appl. Mater. Interfaces* **2013**, *5*, 3867–3874.
[49] S. Morrison, T. Freund, *J. Chem. Phys.* **1967**, *47*, 1543–1551.
[50] S. Sakthivel, B. Neppolian, M. Shankar, B. Arabindoo, M. Palanichamy, V. Murugesan, *Sol. Energy Mater. Sol. Cells* **2003**, *77*, 65–82.
[51] S. Chakrabarti, B. K. Dutta, *J. Hazard. Mater.* **2004**, *112*, 269–278.
[52] C. J. Youn, T. S. Jeong, M. S. Han, J. H. Kim, *J. Cryst. Growth* **2004**, *261*, 526–532.
[53] J. Zhou, N. S. Xu, Z. L. Wang, *Adv. Mater.* **2006**, *18*, 2432–2435.
[54] Y. Zhang, Z. Chen, S. Liu, Y.-J. Xu, *Appl. Catal. B* **2013**, *140–141*, 598–607.
[55] H. A. Foster, I. B. Ditta, S. Varghese, A. Steele, *Appl. Microbiol. Biotechnol.* **2011**, *90*, 1847–1868.
[56] A. Sirelkhatim, S. Mahmud, A. Seeni, N. H. M. Kaus, L. C. Ann, S. K. M. Bakhori, H. Hasan, D. Mohamad, *Nano-Micro Lett.* **2015**, *7*, 219–242.
[57] L. Hui, J.-G. Piao, J. Auletta, K. Hu, Y. Zhu, T. Meyer, H. Liu, L. Yang, *ACS Appl. Mater. Interfaces* **2014**, *6*, 13183–13190.

[58] Y.-W. Wang, A. Cao, Y. Jiang, X. Zhang, J.-H. Liu, Y. Liu, H. Wang, *ACS Appl. Mater. Interfaces* **2014**, *6*, 2791–2798.
[59] P. Li, S. Sun, A. Dong, Y. Hao, S. Shi, Z. Sun, G. Gao, Y. Chen, *Appl. Surf. Sci.* **2015**, *355*, 446–452.
[60] Z. Yang, X. Hao, S. Chen, Z. Ma, W. Wang, C. Wang, L. Yue, H. Sun, Q. Shao, V. Murugadoss, Z. Guo, *J. Colloid Interface Sci.* **2019**, *533*, 13–23.
[61] A. J. Lopatkin, J. M. Stokes, E. J. Zheng, J. H. Yang, M. K. Takahashi, L. You, J. J. Collins, *Nat. Microbiol.* **2019**, *4*, 2109–2117.
[62] Y. Tao, Y. Wang, S. Huang, P. Zhu, W. E. Huang, J. Ling, J. Xu, *Anal. Chem.* **2017**, *89*, 4108–4115.

Manuscript received: July 28, 2020
Revised manuscript received: September 1, 2020
Version of record online: September 25, 2020

